Kang Shu
Tribology Research Institute,
State Key Laboratory of Traction Power,
Southwest Jiaotong University,
Chengdu 610031, China
e-mail: 642593287@qq.com

Wen-Jian Wang
Tribology Research Institute,
State Key Laboratory of Traction Power,
Southwest Jiaotong University,
Chengdu 610031, China
e-mail: wwj527@swjtu.cn

Enrico Meli
Department of Industrial Engineering,
University of Florence,
Firenze 50139, Italy
e-mail: enrico.meli@unifi.it

Hao-Hao Ding[1]
Tribology Research Institute,
State Key Laboratory of Traction Power,
School of Mechanical Engineering,
Southwest Jiaotong University,
Chengdu 610031, China
e-mail: haohao.ding@swjtu.edu.cn

Zhen-Yu Han
Pangang Group Panzhihua Iron and Steel
Research Institute Co. Ltd.,
Panzhihua 617000, China
e-mail: 695205784@qq.com

Ming Zou
Pangang Group Panzhihua Iron and Steel
Research Institute Co. Ltd.,
Panzhihua 617000, China
e-mail: 1479168080@qq.com

Qi-Yue Liu
Tribology Research Institute,
State Key Laboratory of Traction Power,
Southwest Jiaotong University,
Chengdu 610031, China
e-mail: 930492730@qq.com

Study on the Influence of Sand Erosion Process on the Wear and Damage of Heat-Treated U75V Rail Steel

Usually, rail materials are exactly affected by the erosion of windblown sand in the desert environment. For this reason, the influence of impact angle, particle velocity, and particle size on the erosion wear behavior of the U75V heat-treated rail steel, a material frequently employed in Chinese railways, were studied in this work. The results showed that, with increasing impact angle, the erosion rate increased between 15 deg and 45 deg, decreased between 45 deg and 75 deg, and then increased again between 75 deg and 90 deg. The highest erosion rate occurred at about 45 deg. When the particle velocity increased, the erosion rate increased approximately in a quadratic way. As the sand particle size increased, the erosion rate presented a decreasing trend. During the initial stage of erosion, shear craters, indentation craters, and ploughing craters were the main surface damage features. The shear craters predominated at the impact angle of 45 deg whereas the indentation craters predominated at 90 deg. During the steady-state of erosion, the rail damage was mainly composed of craters, platelets, and cracks. Both the length and depth of craters increased almost linearly with increasing particle velocity, whereas the increased rate of length was significantly higher than that of depth. The length and depth of craters increased with increasing particle size at 90 deg, whereas only the length increased with increasing particle size at 45 deg. The microstructure evolution and the formation mechanism of platelet at low impact angles were different from those at high impact angles. Platelet formation was the main erosion wear mechanism.
[DOI: 10.1115/1.4049110]

Keywords: cutting, erosion, indentation, surfaces, wear mechanisms

1 Introduction

Because of the rapid development of railways transportation, the service environmental conditions of rails became harsher. In many regions, such as the Middle East, the North Africa, and the Western China, many railways run through arid and desert areas [1], where the rails have been suffering serious erosion of windblown sand, as shown in Fig. 1 [2]. The rail surfaces can be damaged by the sand particles, and the damage can deteriorate in the following service and finally threaten the service safety of the railway line.

However, few studies on the erosion behaviors of rail steels in realistic windblown sand environments have been carried out so far. Previous studies have been performed to explore the solid particle erosion behaviors on different types of materials. They showed that the solid particle erosion process was closely related to many parameters including impact angle, particle velocity of erodent, and particle size of erodent [3,4]. Erosion rate (E) is widely used to evaluate the erosion resistance of materials and is often defined as the mass loss of the target material divided by the mass of erodent particles. The effect of the impact angle on the erosion behaviors of the target material deeply depends on the nature of the material [5]. In general, the impact angle corresponding to the highest erosion rate is in the range 15–30 deg for ductile materials, such as steels [6–13], aluminum alloys [14–16], Ti–6Al–4V alloy [14,17,18], high-velocity oxy-fuel (HVOF) coatings [19], glass fiber, and epoxy composites [20,21], whereas it is about 90 deg for brittle materials, such as sodalime glass and Pyrex glass [22], ceramics and ceramic composites [23], concrete materials [24]. Particle velocity of erodent is another significant parameter influencing the erosion behavior. The erosion rate of the target material varies with the particle velocity according to a power

[1]Corresponding author.

Contributed by the Tribology Division of ASME for publication in the Journal of Tribology. Manuscript received September 7, 2020; final manuscript received November 9, 2020; published online December 14, 2020. Assoc. Editor: Yi Zhu.

Fig. 1 Railway in the windblown sand environment [2]

law: $E = kV^n$, where k is a constant depending on the material, V is the particle velocity of the erodent, and n is the velocity exponent of the specific erodent. The value of n for ductile materials is about 2.0–2.7, as reported in previous works [8,25,26]. In addition, the particle size of erodent is an influencing factor for erosion behavior as well. Sheldon [25] reported that the erosion rate of target material changed with the particle size according to a power law and the particle size exponent for ductile materials (such as annealed tool steel) was about 3. However, Tilly [26] found that the erosion rate presented an increasing trend with increasing particle size until the particle size reached a limit value; after that, the erosion rate remained relatively stable as the particle size increased further. Besides, the correlation between erosion rate and particle size was different for different steels [27]. Therefore, particle size has a relatively complicated effect on the erosion rate.

Heat-treated U75V rail steel is one of the most widely used rail steels on high-speed and heavy-haul lines in China due to its good wear resistance. However, the sand erosion behavior of this rail steel in the presence of windblown sand is still unknown. Accordingly, the purpose of the current work is to investigate the erosion behavior of the heat-treated U75V rail steel in realistic windblown sand environments. To this end, the influence of the impact angle, the particle velocity, and the particle size on sand erosion behavior of the rail steel was carefully explored experimentally. The erosion rate, surface damage, and subsurface damage were analyzed in detail. Furthermore, the microstructure evolution and sand erosion mechanism of heat-treated U75V rail steel were discussed as well.

2 Experimental Details

2.1 Materials

2.1.1 Rail Specimen. Rail specimens for the erosion tests were taken from the heat-treated U75V rail. The mechanical properties and chemical compositions of the rail steel are detailed in Table 1. All rail specimens were cut from the rail head and the dimensions of specimen are illustrated in Fig. 2(*a*). In order to observe and analyze the erosion behavior of the rail steel clearly, the upper surface of the rail specimen was grounded through SiC abrasive papers and then polished by means of diamond abrasion paste until its roughness reached 0.06 ± 0.01 μm. Figure 2(*b*) shows that the microstructure of the rail steel is mainly lamellar pearlite. The mean interlamellar spacing is about 116 nm.

2.1.2 Erodent Particles. To make the experimental conditions closer to those in the field, the sand was selected as the best erodent material for the erosion tests and was directly collected from the Gobi region near the south Xinjiang railway in China. The sand is composed primarily of SiO_2. The hardness of the sand is about 7 Mohs. The original sand is named R sand in the present work. Figure 3(*a*) shows the distribution of particle sizes of the R sand, obtained by using a laser particle size analyzer (Mastersizer 2000, Worcestershire, UK). The original sand (R sand) was sifted into three groups of sand particles with different size ranges: small sand (20–250 μm, named S sand), middle sand (250–500 μm, named M sand), and large sand (500–1700 μm, named L sand). The proportions of S sand, M sand, and L sand in the R sand are shown in Fig. 3(*b*). The mean diameters of R sand, S sand, M sand, and L sand are around 277 μm, 171 μm, 366 μm, and 730 μm, respectively. The optical micrographs of these four types of sands (Fig. 4) reveal that the sand particles have irregular shapes and different colors.

2.2 Erosion Testing. Based on the ASTM G76-95 standard test method [28] and the real characteristics of windblown sand environment, an erosion testing machine was specially designed for the sand erosion tests of the rail steel, as shown in Fig. 5. The sand particles flowed through the sand trap (6), then were sucked into the sandblasting gun (3), accelerated by the high-speed airflow in the nozzle, and finally struck the surface of rail specimen (7). The erosion tester was able to control several variables such as the impact angle, the particle velocity, and the feed rate of erodent particles. The impact angle can be changed by rotating the specimen holder (8). The particle velocity can be changed by adjusting the pressure regulating valve (2) and was determined by using the double-disc method [29]. The erodent particles feed rate can be controlled by adjusting the sand trap (6).

The erosion testing fixed conditions are specified in Table 2. Three series of tests were carried out with six impact angles (15 deg, 30 deg, 45 deg, 60 deg, 75 deg, and 90 deg), five particle velocities (13, 20, 27, 34, and 41 m/s) [30,31], and four types of particle size (R sand, S sand, M sand, and L sand), as shown in Table 3. The relationship between the particle velocity and the applied air jet pressure is shown in Table 4. Although the sand (especially R sand) used in the erosion tests had a large range of particle sizes, the velocities of particles with different sizes were pretty similar to each other because saturated acceleration was available for these sand particles relying on the suction force and thrust force of the high-speed airflow.

Before and after each erosion test, the rail specimens were immersed in ethanol, washed with an ultrasonic cleaner, dried, and weighed by a digital balance with a resolution of 0.1 mg (JJ324BC, Shanghai, China). Each erosion test under the same conditions was repeated at least twice. After the erosion tests, the damaged surfaces and the cross sections were cut from the specimens. The cross sections were embedded in resin, grounded and

Table 1 Mechanical properties and chemical composition (wt%) of the rail steel

Heat-treated U75V rail steel						
Tensile strength (MPa)			≥ 1180			
Percentage elongation after fracture (%)			≥10			
Hardness ($HV_{0.5}$)			366±7			
Composition						
C	Si	Mn	P	S	V	Al
0.71–0.80	0.50–0.80	0.70–1.05	≤ 0.030	≤ 0.025	0.04–0.12	≤ 0.010

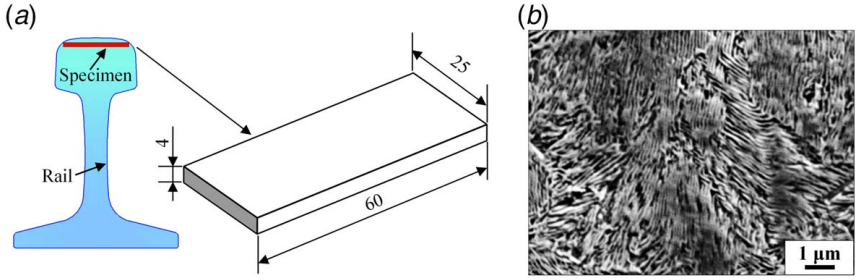

Fig. 2 Details of the rail specimen: (*a*) sampling position and dimensions (mm) of the rail specimen and (*b*) microstructure of the rail steel

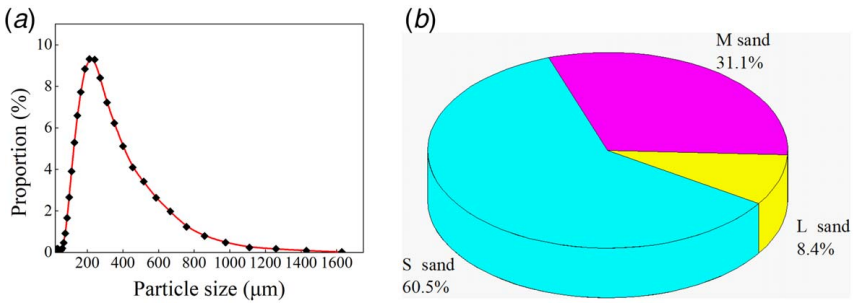

Fig. 3 Sizes of the sand particles: (*a*) distribution of particle sizes of the R sand and (*b*) proportions of the S sand, M sand, and L sand in the R sand

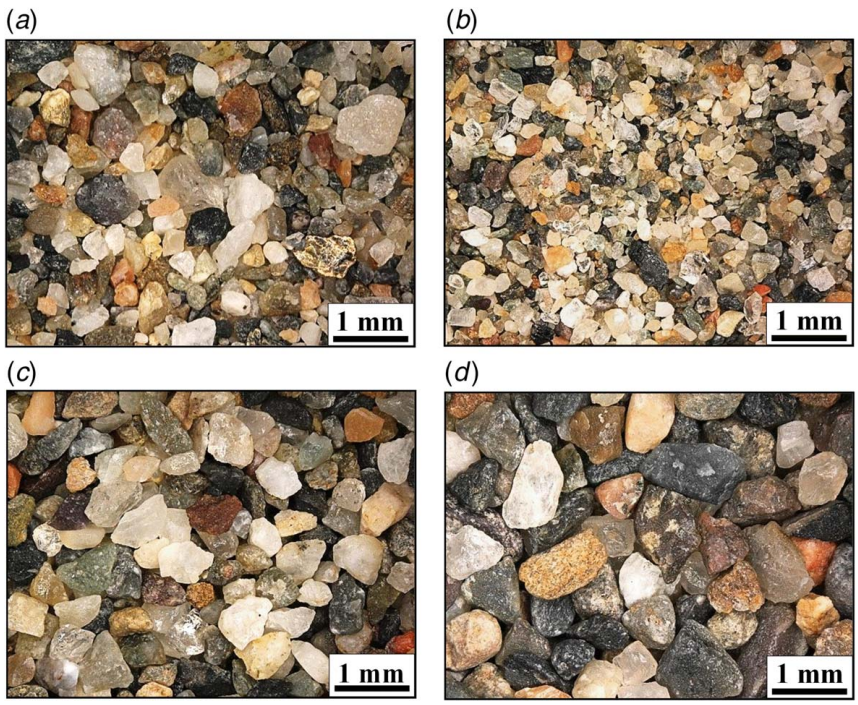

Fig. 4 Optical micrographs of the sands: (*a*) R sand (20–1700 μm), (*b*) S sand (20–250 μm), (*c*) M sand (250–500 μm), and (*d*) L sand (500–1700 μm)

polished, and then etched with a 4% nital solution. The damaged surfaces and cross sections were analyzed using a scanning electron microscope (SEM) (Phenom Pro-SE, Eindhoven, The Netherlands).

3 Results and Discussion

3.1 Erosion Rate. Figure 6 shows the variation of the mass loss of the rail as a function of the erosive time at different impact angles. It is clear that the mass loss increased unsteadily with the increase in erosive time during the initial stage and then increased almost linearly, whereas the erosion rate is the rate of the mass loss of the rail with respect to the mass of sand which is the product of the sand particles feed rate and the erosive time. Therefore, it also means that the erosion rate fluctuated during the initial stage and then tended to steady. Simultaneously, steady-state erosion rate can also be obtained from the slope at the steady-state.

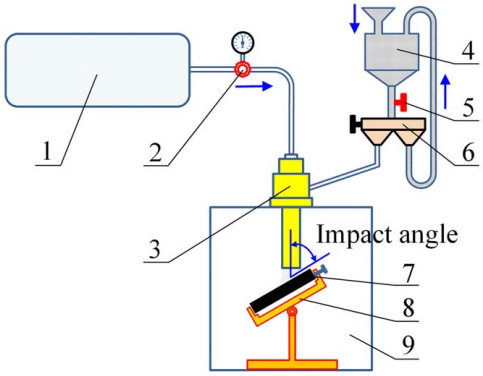

Fig. 5 Schematic diagram of the erosion testing machine: (1) compressed air, (2) pressure regulating valve, (3) sandblasting gun, (4) sand storage hopper, (5)sand regulating valve, (6) sand trap, (7) specimen, (8) specimen holder, and (9) Erosion chamber

Table 2 Erosion testing fixed conditions

Erosion testing conditions	
Sand particles feed rate (g/min)	10
Mass loss measurement intervals (min)	8
Nozzle inner diameter (mm)	9.3
Nozzle to specimen distance (mm)	10
Nozzle length (mm)	274
Test temperature	Room temperature
Test gas	Dry compressed air

Table 3 Erosion testing variable parameters

Series	Impact angle (deg)	Particle velocity (m/s)	Particle size (mm)
1	15, 30, 45, 60, 75, 90	20	R
2	45, 90	13, 20, 27, 34, 41	R
3	45, 90	20	S, M, L, R

Table 4 Air jet pressure versus particle velocity

Air jet pressure (bar)	0.4	0.8	1.1	1.6	1.8
Particle velocity (m/s)	13	20	27	34	41

The erosion rate in the following sections is referred to as the erosion rate at the steady-state.

3.1.1 Effect of Impact Angle on Erosion Rate. Figure 7 illustrates the correlation between erosion rate and impact angle for the R sand and the particle velocity of 20 m/s. It is clear that when the impact angle increased, the erosion rate increased as well first, reaching a maximum at about 45 deg. Subsequently, the erosion rate dropped until reaching a minimum at about 75 deg, afterward it increased again between 75 deg and 90 deg. The highest erosion rate occurred at 45 deg in this study, whereas it usually occurs at impact angles between 15 deg and 30 deg for ductile materials. The evolution trend of the erosion rate as a function of the impact angle of the U75V rail steel was quite similar to that of heat-treated 1078 steel consisting of fine pearlite microstructure [8]. It is known that the material microstructure has a significant influence on the cutting and deformation properties. At the same time, the erosion wear of the materials is usually caused by cutting wear and repeated deformation wear [32]. Therefore, it is reasonable that the correlation between erosion rate and impact angle was significantly affected by the microstructure of the material.

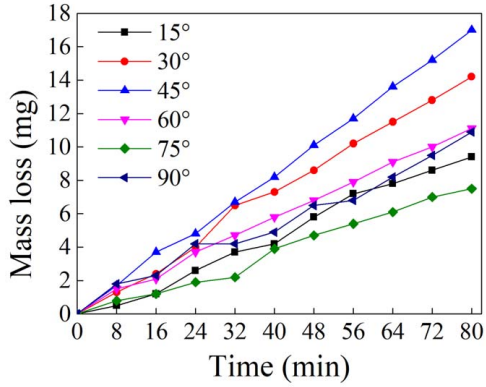

Fig. 6 Variation of the mass loss of the rail as a function of the erosive time at different impact angles (R sand; particle velocity of 20 m/s)

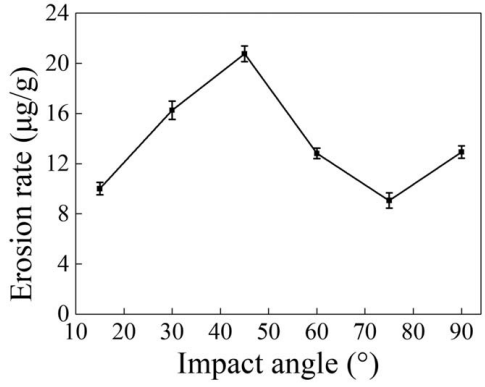

Fig. 7 Correlation between erosion rate and impact angle (R sand; particle velocity of 20 m/s)

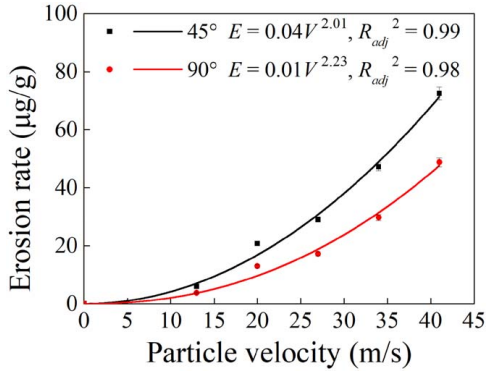

Fig. 8 Correlation between erosion rate and particle velocity at 45-deg and 90-deg impact angles (R sand)

3.1.2 Effect of Particle Velocity on Erosion Rate. Figure 8 shows the correlation between erosion rate and particle velocity for the R sand at the impact angles of 45 deg and 90 deg. The erosion rate increased significantly with increasing particle velocity. For instance, the erosion rate at 41 m/s is approximately 13 times the rate at 13 m/s. This was mainly because the sand particles with higher velocity had greater kinetic energy, resulting in greater impact stress when they struck the rail surface, which made easier the removal of the rail material. In addition, the erosion rate at 45 deg was always larger than that at 90 deg under the same conditions. The experimental curves were fitted using the Least-squares Algorithm, and a power-like correlation

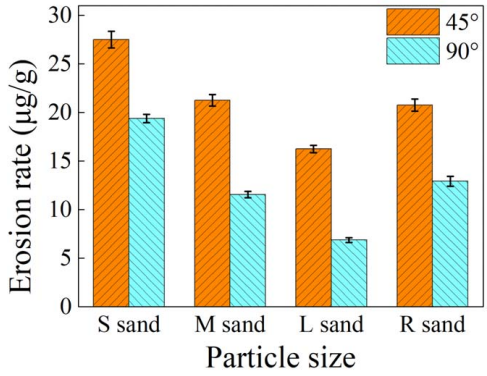

Fig. 9 Correlation between erosion rate and particle size at the impact angles of 45 deg and 90 deg (particle velocity of 20 m/s)

between erosion rate and particle velocity was found: $E = kV^n$. The fitted curves had an excellent fitting degree with the actual data. The k and n parameters at the impact angle of 45 deg were 0.04 and 2.0, respectively, whereas the k and n values at 90 deg were 0.01 and 2.2, respectively. The values of n were both in the range between 2 and 3, which is consistent with that of ductile materials in previous works [8,25,26,33,34].

3.1.3 Effect of Particle Size on Erosion Rate. Figure 9 shows the erosion rates with different sizes of sand particles at the impact angles of 45 deg and 90 deg (particle velocity of 20 m/s). The erosion rate decreased with increasing particle size. Additionally, the erosion rate of the R sand was similar to that of the M sand. The trend of the erosion rate with particle size was consistent with that in Ref. [27]. A possible explanation is that the number of the sand particles decreases if the particle size increases (for the same mass of sand); thus, the number of the impacts on the same spot of the rail surface decreases with increasing particle size, which results in a lower material removal capacity for larger sand particles although the total kinetic energy is still the same for the same mass of sand with different sizes.

Figure 9 also shows that the erosion rate at 45 deg was always greater than that at 90 deg as expected. This was mainly because the shear stress and normal stress were simultaneously produced on the specimen surface at low impact angles whereas the normal stress was mainly produced at high impact angles [35]. Another reason for this trend was that the probability of rebounding particles and fragments colliding with incoming particles at low impact angles is lower than that at high impact angles. Such collisions could lead to a loss of kinetic energy and change direction of the incoming particles [36], affecting the capability of material removal. The erosion rates with S sand, M sand, and L sand at 45 deg were 42%, 84%, and 136% larger than those at 90 deg, respectively. It showed that the difference in erosion rate between 45 deg and 90 deg increased with increasing particle size. The results also revealed that the erosion rate at 45 deg was less sensitive to the particle size than that at 90 deg.

3.2 Surface Damage of the Rail Steel

3.2.1 Surface Damage During the Initial Stage. In order to explore the surface damage of the rail during the initial stage, erosion tests of series 3 in Table 3 were conducted for 3 sec. Figures 10 and 11 show the SEM photographs of damaged surfaces in the initial stage at 45 deg and 90 deg (particle velocity of 20 m/s), respectively.

It is shown in Fig. 10 that after the test at 45 deg, the shear crater was the most principal damage feature in the initial stage, and the size of the shear crater increased with increasing particle size. Ploughing crater and indentation crater were also observed on the damaged surfaces (e.g., Figs. 10(*a*)–10(*c*)). In Fig. 10(*d*), a thick lip was formed at the end of the shear crater due to the shear action of an L sand particle with a large particle size. In addition, some shallow ploughing craters were generated at the bottom of

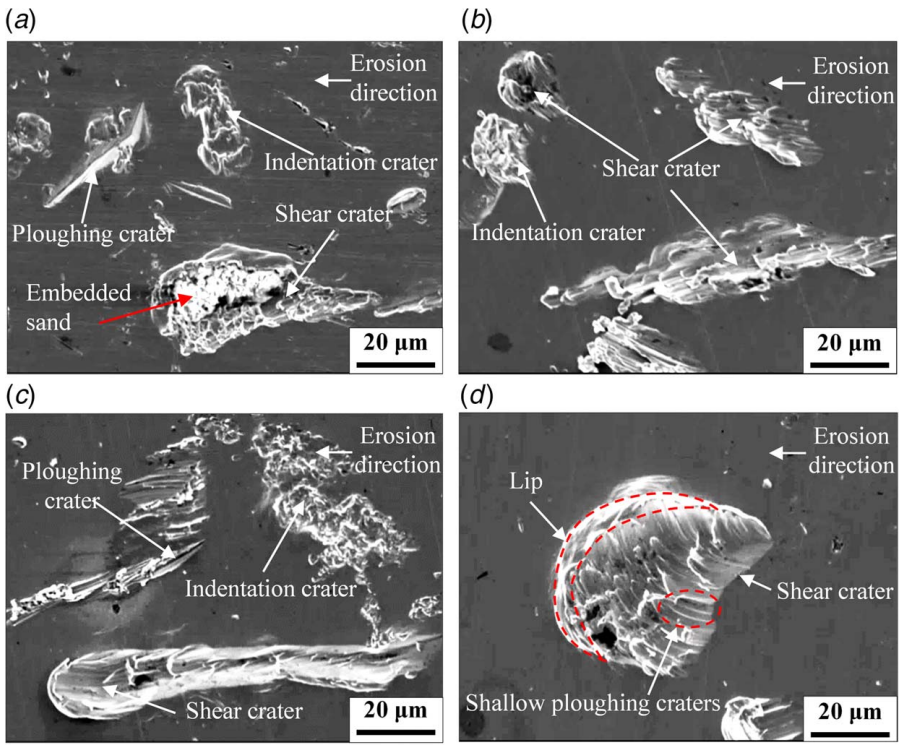

Fig. 10 SEM photographs of the damaged surfaces during the initial stage at 45-deg impact angle (particle velocity of 20 m/s): (*a*) R sand, (*b*) S sand, (c) M sand, and (*d*) L sand

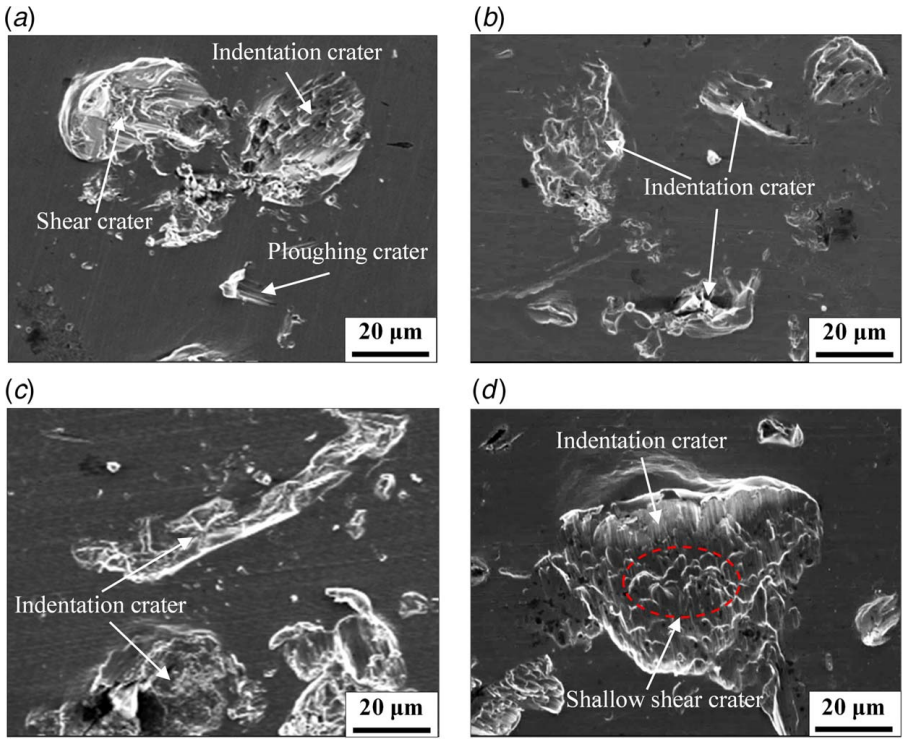

Fig. 11 SEM photographs of the damaged surfaces during the initial stage at 90-deg impact angle (particle velocity of 20 m/s): (*a*) R sand, (*b*) S sand, (c) M sand, and (*d*) L sand

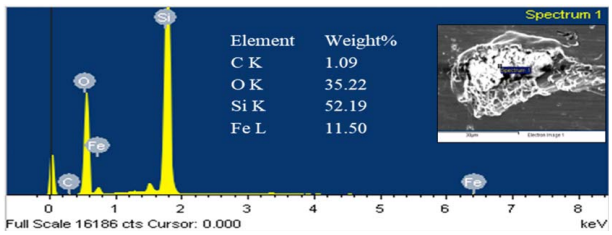

Fig. 12 SEM-EDS analysis of the material embedded into the damaged surface

the shear crater, which was mainly caused by the irregular shape of the sand particle.

It is clear from Fig. 11 that, after the test at 90 deg, the indentation crater was the most important damage feature during the initial stage, and the size of the shear crater increased when the particle size increased. Shear crater and ploughing crater can also be observed on the damaged surface (e.g., Fig. 11(*a*)). Besides, a long indentation crater was observed in Fig. 11(*c*). It may also be caused by an M sand particle with a long shape. In Fig. 11(*d*), a large number of shallow shear craters were generated at the bottom of the indentation crater due to the irregular shape of sand particles.

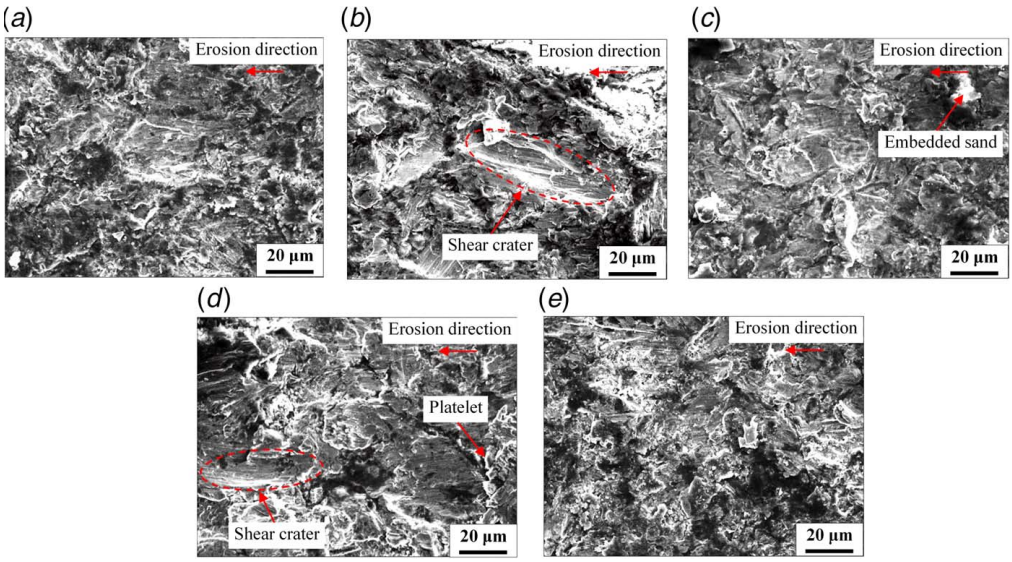

Fig. 13 SEM photographs of the damaged surfaces during the steady-state with different particle sizes and particle velocities at 45-deg impact angle: (*a*) R sand, 20 m/s, (*b*) R sand, 34 m/s, (c) S sand, 20 m/s, (*d*) M sand, 20 m/s, and (e) L sand, 20 m/s

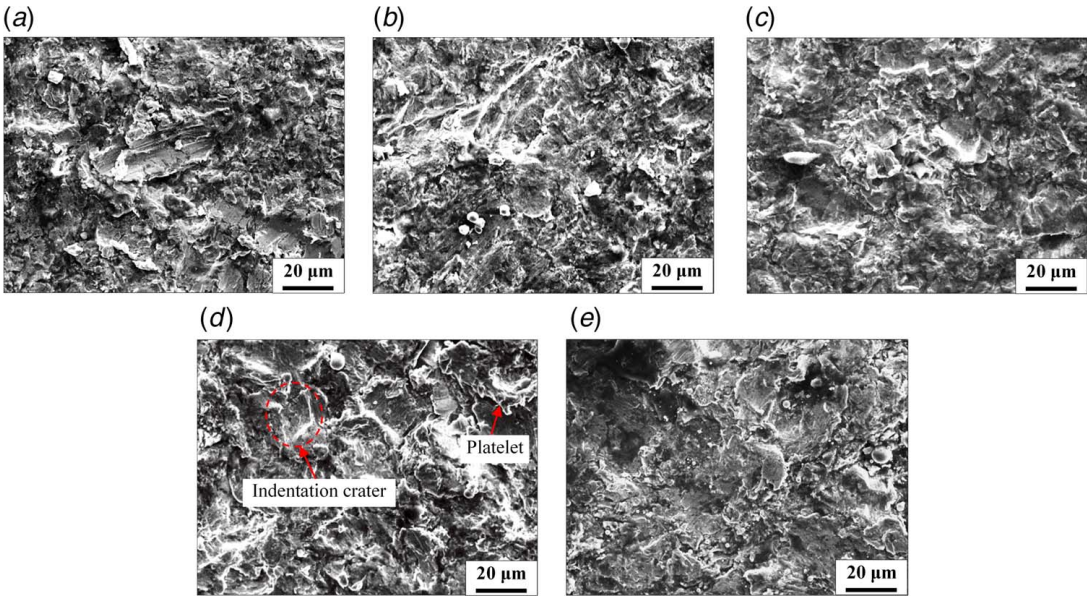

Fig. 14 SEM photographs of the damaged surfaces during the steady-state with different sand particle sizes and particle velocities at 90 deg impact angle: (*a*) R sand, 20 m/s, (*b*) R sand, 34 m/s, (c) S sand, 20 m/s, (*d*) M sand, 20 m/s, and (*e*) L sand, 20 m/s

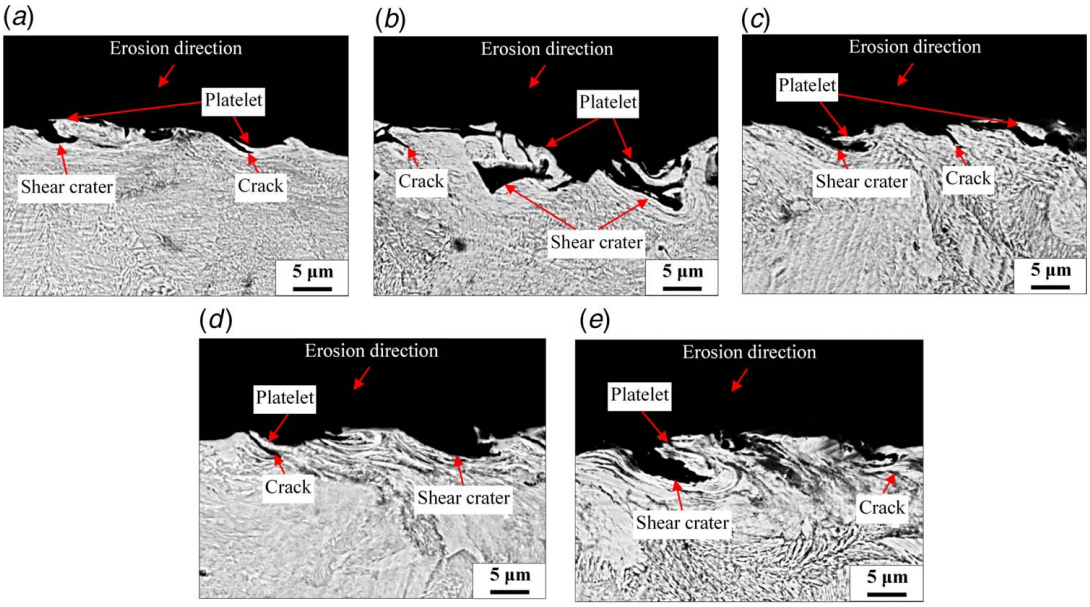

Fig. 15 SEM photographs of the damaged cross sections during the steady-state with different sand particle sizes and particle velocities at 45-deg impact angle: (*a*) R sand, 20 m/s, (*b*) R sand, 34 m/s, (c) S sand, 20 m/s, (*d*) M sand, 20 m/s, and (e) L sand, 20 m/s

Comparing the surface damages during the initial stage at impact angles of 45 deg and 90 deg, it can be concluded that three types of craters (shear crater, indentation crater, and ploughing crater) can be formed on the surface, which were mainly caused by the different impact angles of the individual particles [37]. Shear crater predominated at the impact angle of 45 deg, whereas indentation crater predominated at 90 deg. In both the cases, the size of the craters increased when the particle size increased.

Furthermore, many small sand particles were embedded into the damaged surface (e.g., Fig. 10(*a*)). Figure 12 shows that the principal elements of material embedded into the surface were Si and O using scanning electron microscope-energy disperse spectroscopy (SEM-EDS) analysis. It demonstrates that the main material embedded into the damaged surface was sand particle (or its fragment) as expected.

3.2.2 Surface Damage During the Steady-State. Figures 13 and 14 show the SEM photographs of the surface damages during the steady-state at the impact angles of 45 deg and 90 deg, respectively. It can be observed from Fig. 13 that the surface damage in the steady-state at an impact angle of 45 deg consisted mainly of shear craters with different sizes and various platelets. Figures 13(*a*) and 13(*b*) show the damaged surfaces caused by R sand with particle velocities equal to 20 m/s and 34 m/s, respectively. The depth of

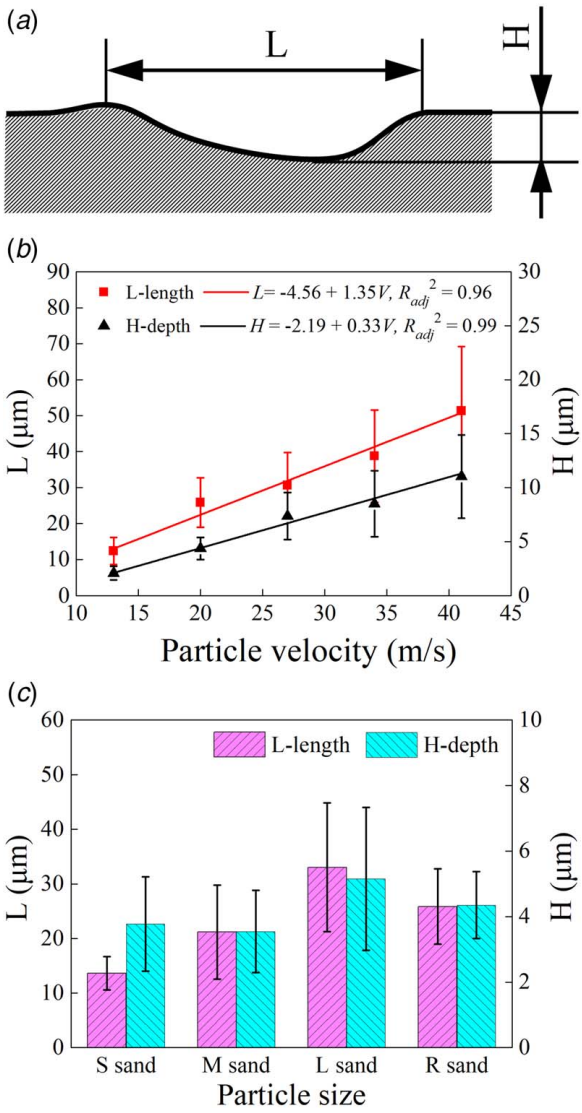

Fig. 16 (*a*) The scheme of the shear crater at 45-deg impact angle: *L*—length of shear crater, *H*—depth of shear crater, (*b*) correlation between the shear crater dimensions and particle velocity at 45-deg impact angle (R sand), and (c) correlation between the shear crater dimensions and particle size at the impact angles of 45 deg (particle velocity of 20 m/s)

the shear crater increased with increasing particle velocity. On the other hand, Figs. 13(*c*)–13(*e*) show the surfaces damaged by S sand, M sand, and L sand, respectively, with a particle velocity equal to 20 m/s. It can be observed that there was no significant difference in the surface damage feature among these three types of sand during the steady-state, even if the crater dimensions increased with the increase in particle size during the initial stage. Besides, the embedded sand particles were also observed on the damaged surface during the steady-state (e.g., Fig. 13(*c*)).

It can be seen from Fig. 14 that the surface damage during the steady-state at the impact angle of 90 deg consisted mainly of indentation craters with different sizes and various platelets. Figures 14(*a*) and 14(*b*) show the surfaces damaged by R sand at the particle velocities of 20 m/s and 34 m/s, respectively. There was no evident difference in the surface damage feature when eroded by sand with different particle velocities. Figures 14(*c*)–14(*e*) show the surfaces damaged by S sand, M sand, and L sand, respectively, with particle velocity equal to 20 m/s. It can be observed that the surface damage features produced by S sand and M sand were quite similar. However, the damage surface created by L sand was much cleaner than those caused by S sand and M sand. This was probably because the contact area between sand particle and specimen increased with increasing particle size.

3.3 Subsurface Damage During the Steady-State. Figure 15 shows the SEM photographs of the cross sections of the damaged rail during the steady-state at the impact angle of 45 deg. It is clear that shear craters, platelets, and cracks were formed on the cross sections produced by different particle velocities and different particle sizes. Shear craters were adjacent to each other along the rail specimen surface and their shapes were quite similar. It is evident that the material near the specimen surface, especially at the bottom of the shear craters, exhibited plastic flow, where the pearlite interlamellar spacing was much smaller than that of the matrix material. Platelets had significant differences in size and shape, and most of the platelets were generated above the end (right side) of the shear craters. Cracks mainly occurred at the bottom of the shear craters, and their orientations were roughly parallel to those of the plastic flows. Figures 15(*a*) and 15(*b*) show the subsurface damages caused by R sand with particle velocities of 20 m/s and 34 m/s, respectively. The dimensions of shear craters and the size of platelets significantly increased with increasing particle velocity. On the other hand, Figs. 15(*c*)–15(*e*) shows the subsurface damages due to S sand, M sand, and L sand, respectively, with a particle velocity of 20 m/s. The dimensions of shear crater appeared to increase with increasing particle size.

In order to better understand the correlation between shear crater dimensions and particle velocity, particle size, the dimensions of shear craters under various conditions were measured as shown in Fig. 16. Figure 16(*a*) shows the scheme of length (L) and depth (H) of the shear crater at 45-deg impact angle. Figure 16(*b*) shows the correlation between the shear crater dimensions and particle velocity. Both the length (L) and the depth (H) of the shear crater increased almost linearly when the particle velocity increased, whereas the increase rate (i.e., the slope of the curve) of the length was significantly higher than that of the depth. On the other hand, Fig. 16(*c*) shows the correlation between the shear crater dimensions and particle size. The length of the shear crater increased with increasing particle size. However, the depths of shear crater caused by S sand and M sand were quite similar, and the depth caused by L sand was the highest. In addition, both the length and depth caused by R sand fell in between those caused by M sand and L sand.

Figure 17 shows that indentation craters, platelets, and cracks can be observed on the cross sections of damaged rail at the impact angle of 90 deg as well. Indentation craters had semi-circular arc shapes, and these craters were covered by platelets with different sizes and shapes. Figures 17(*a*) and 17(*b*) show the subsurface damage caused by R sand with particle velocities of 20 m/s and 34 m/s, respectively. Both the dimensions of the indentation craters and the size of the platelets significantly increased with increasing the particle velocity, which was consistent with the fact that the sand with higher particle velocity can lead to a higher erosion rate. Figures 17(*c*)–17(*e*) show the subsurface damages due to S sand, M sand, and L sand, respectively, with a particle velocity of 20 m/s. There was some difference in the dimensions of indentation crater created by these three types of sand. As shown in Fig. 18, the dimensions of indentation crater under various conditions were measured as well. Figure 18(*a*) shows the scheme of length (L) and depth (H) of indentation crater at 90-deg impact angle. Figure 18(*b*) shows the correlation between the indentation crater dimensions and particle velocity. Similarly, both the length (L) and the depth (H) of the shear crater increased almost linearly when the particle velocity increased, whereas the increase rate (i.e., the slope of the curve) of the length was significantly higher than that of the depth. On the other hand, Fig. 18(*c*) shows the correlation between the indentation crater dimensions and particle size. Both the length and the depth of the indentation crater increased with increasing particle size, whereas the increase in depth was

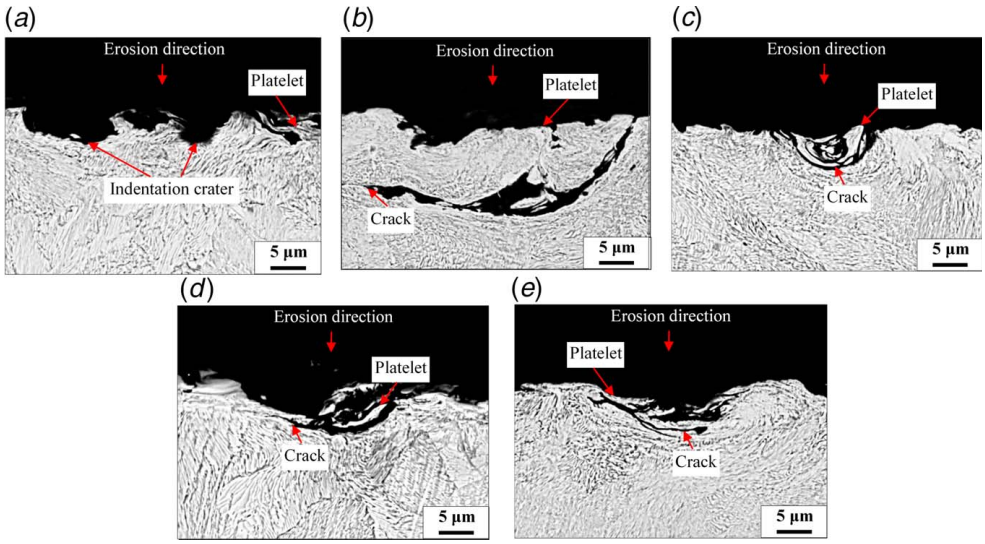

Fig. 17 SEM photographs of the damaged cross sections during the steady-state with different sand particle sizes and particle velocities at 90-deg impact angle: (*a*) R sand, 20 m/s, (*b*) R sand, 34 m/s, (c) S sand, 20 m/s, (*d*) M sand, 20 m/s, and (e) L sand, 20 m/s

relatively slight. In addition, both the length and the depth of the indentation crater caused by R sand were similar to the one created by S sand.

To summarize, comparing the subsurface damages during the steady-state at the impact angles of 45 deg and 90 deg, it can be concluded that craters, platelets, and cracks were the most significant features. Shear craters prevailed at the impact angle of 45 deg, whereas indentation crater predominated at 90 deg. Both the length and depth of craters increased almost linearly with increasing particle velocity, whereas the increase rate of the length was significantly higher than that of the depth. The length and depth of craters increased with increasing particle size at 90 deg, whereas only the length increased with increasing particle size at 45 deg.

3.4 Erosion Wear Mechanism. Different erosion mechanisms for ductile materials were proposed to clarify the material removal processes when solid particles impacted on the material surfaces. In 1960, Finnie [38] reported that the removal of ductile materials was caused by the cutting of solid particles. Afterward, Bitter [32] reported that the wear of materials eroded by solid particles resulted from cutting action and repeated deformation. Furthermore, these two actions occurred simultaneously. Tilly [39] found that the erosion mechanism for ductile materials could be divided into two stages. In the first stage, an indentation was generated, and probably, a small piece of target material was removed when a particle struck the material surface. In the second stage, the secondary damage could be caused by the fragments coming from the breakup of the particle in the first stage. Bellman and Levy [37] found that heavily distressed platelets were formed on the damaged surface of ductile metals due to forging-extrusion action. These platelets would shed from the surface after having suffered the impacts of the subsequent particles, which resulted in the removal of the target material at both low and high impact angles. Later, on the basis of the results observed in the Ref. [37], Levy [9] proposed the platelet mechanism: in this case, thin platelets were produced by extrusion and forging, and then, the platelets shed from the eroded surface subsequently.

Although the erosion wear mechanisms have been well studied, few studies have focused on the evolution of material microstructure in the erosion process. Therefore, in this work, both the rail microstructure evolution in the erosion process and the erosion wear mechanism would be discussed. Combining the analysis of surface damages (Figs. 10 and 13), subsurface damages (Fig. 15),

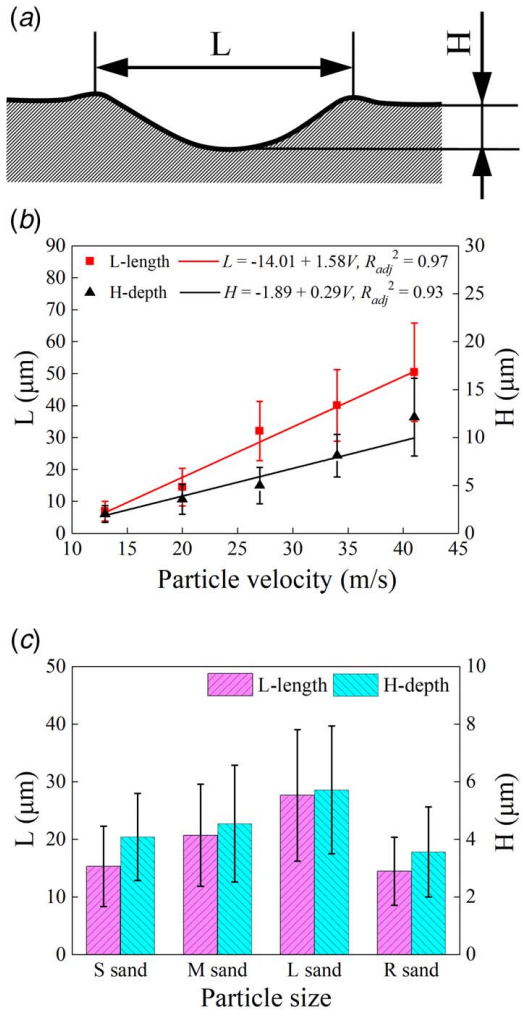

Fig. 18 (*a*) The scheme of the shear crater at 90-deg impact angle: *L*—length of the shear crater, *H*—depth of shear crater, (*b*) correlation between the shear crater dimensions and particle velocity at 90 deg impact angle (R sand), and (c) correlation between the shear crater dimensions and particle size at the impact angles of 90 deg (particle velocity of 20 m/s)

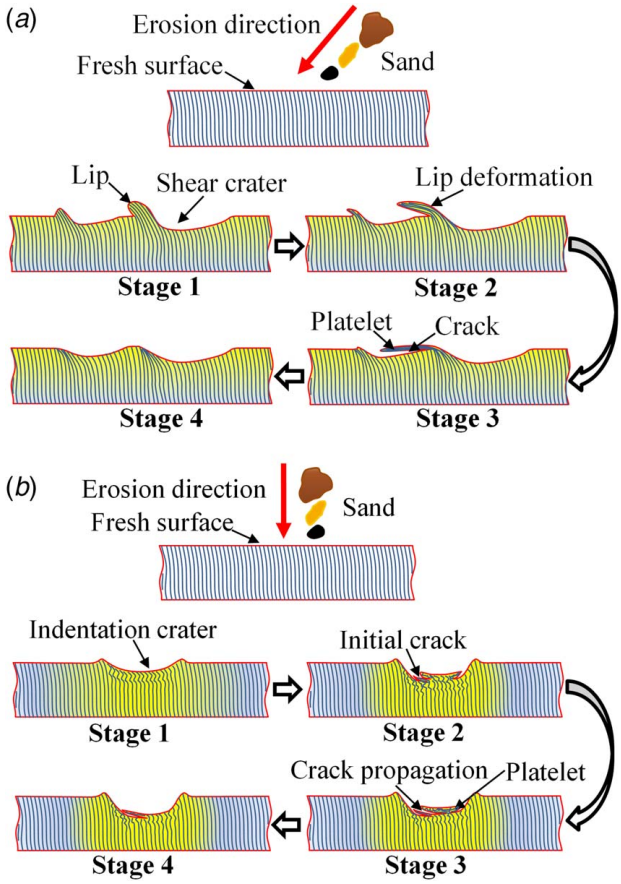

Fig. 19 Schematic diagram of the microstructure evolution and the material removal process at different impact angles: (*a*) low impact angles and (*b*) high impact angles

and the platelet mechanism described in Ref. [9], a schematic diagram of the microstructure evolution and the material removal process for the considered rail steel at low impact angles was proposed in Fig. 19(*a*). The term fresh surface is referred to as the surface of the specimen that has not been eroded yet [37]. As shown in the first stage, the pearlite of the lips was elongated and bent along the erosion direction, and the interlamellar spacing of pearlite was significantly shortened. It led to the formation of some shear craters and lips on the specimen surface. In addition, a small amount of material was removed from the specimen surface. After the impacts of subsequent sand particles, as shown in the second stage, the pearlite of the lips was further elongated and its interlamellar was further shortened, which caused the lip to gradually deform and develop into a platelet. As the platelet continued to be impacted by sand particles, it covered the end of the shear crater resulting in the formation of a crack, as shown in the third stage. The formation mechanism of the crack is different from that of the general crack which is developed from the defects of material. The platelets became distressed, and the pearlite almost reached its critical strain hardening [40,35]. After a certain number of subsequent impacts, the pearlite of the crack tip was fractured, and then, the platelet was shed off from the damaged surface, as shown in the fourth stage.

Whereas the microstructure evolution in the material removal process at high impact angles was different from that at low impact angles. Based on the analysis of surface damages (Figs. 11 and 14), subsurface damages (Fig. 17), and the low-cycle fatigue mechanism described in Refs. [3,6], a schematic diagram of the microstructure evolution and the material removal process at the high impact angle was proposed in Fig. 19(*b*). In the first stage, the pearlite around the bottom of the indentation crater was compressed into a spring shape, and some indentation craters were formed on the surface. As the number of impacts increased, fatigue cracks were generated because the pearlite was repeatedly compressed further and partially reached its critical strain hardening, as shown in the second stage. Subsequently, in the third stage, the fatigue cracks gradually propagated, resulting in the formation of platelets. Finally, the cracks coalesced and then the platelets shed off from the damaged surface of the rail in the fourth stage.

Overall, it can be concluded that the platelet mechanism was the main reason for material removal for the heat-treated U75V rail steel suffering sand erosion, although the microstructure evolution and the formation mechanism of the platelets at low impact angles were different from those at high impact angles.

4 Conclusions and Future Work

Through studying the sand erosion behaviors of heat-treated U75V rail steel at different impact angles, different particle velocities and different particle sizes, the following conclusions were drawn:

(1) The impact angle, particle velocity, and particle size significantly affected the erosion rate of the rail steel. With the impact angle increased, the erosion rate increased between 15 deg and 45 deg first, and then declined between 45 deg and 75 deg, afterwards, increased between 75 deg and 90 deg. The highest erosion rate occurred at 45 deg. The erosion rate increased with increasing particle velocity according to a power function with the velocity exponent of about 2. The erosion rate declined with increasing particle size.

(2) In the initial stage of sand erosion, three types of craters (shear crater, indentation crater and ploughing crater) were the main surface damage features. The shear crater predominated at the impact angle of 45 deg while the indentation crater predominated at 90 deg. The size of the crater increased with increasing particle size.

(3) In the steady-state of sand erosion, the surface damage consisted mainly of craters with different sizes and various platelets. The most significant features of subsurface damage were crater, platelet, and crack. As the particle velocity increased, both the depth of the crater and the size of the platelet increased significantly. The depth of the crater increases with increasing particle size at 45 deg, while the increase is not obvious at 90 deg.

(4) Although the microstructure evolution and the formation mechanism of the platelets at low impact angles were different from those at high impact angles, the platelet mechanism was the predominant mechanism for the material removal of heat-treated U75V rail steel suffering sand erosion.

In this work, the erosion behavior of the rail steel in the windblown sand environment was been investigated. The rolling contact fatigue behaviors of the wheel and rail steels under the rolling-sliding contact in the windblown sand environment will be investigated in the future.

Acknowledgment

This work was supported by the National Natural Science Foundation of China (Grant Nos. 51775455 and 51975489), China Postdoctoral Science Foundation (Grant No. 2019M663548) and Fundamental Research Funds for the Central Universities (Grant No. 2682020CX29).

Conflict of Interest

There are no conflicts of interest.

Data Availability Statement

The authors attest that all data for this study are included in the paper.

References

[1] Bruno, L., Horvat, M., and Raffaele, L., 2018, "Windblown Sand Along Railway Infrastructures: A Review of Challenges and Mitigation Measures," J. Wind Eng. Ind. Aerodyn., **177**, pp. 340–365.

[2] Railway Education and Training, 2017, "Can the Train in the Desert Still Run When the Sandstorm Suddenly Comes?"

[3] Finnie, I., 1972, "Some Observations on the Erosion of Ductile Metals," Wear, **19**(1), pp. 81–90.

[4] Jafari, A., and Abbasi Hattani, R., 2020, "Investigation of Parameters Influencing Erosive Wear Using DEM," Friction, **8**(1), pp. 136–150.

[5] Sundararajan, G., and Manish, R., 1997, "Solid Particle Erosion Behaviour of Metallic Materials at Room and Elevated Temperatures," Tribol. Int, **30**(5), pp. 339–359.

[6] Levy, A. V., 1981, "The Solid Particle Erosion Behavior of Steel as a Function of Microstructure," Wear, **68**(3), pp. 269–287.

[7] Foley, T., and Levy, A., 1983, "The Erosion of Heat-Treated Steels," Wear, **91**(1), pp. 45–64.

[8] McCabe, L. P., Sargent, G. A., and Conrad, H., 1985, "Effect of Microstructure on the Erosion of Steel by Solid Particles," Wear, **105**(3), pp. 257–277.

[9] Levy, A. V., 1986, "The Platelet Mechanism of Erosion of Ductile Metals," Wear, **108**(1), pp. 1–21.

[10] Aminul Islam, M., Farhat, Z. N., Ahmed, E. M., and Alfantazi, A. M., 2013, "Erosion Enhanced Corrosion and Corrosion Enhanced Erosion of API X-70 Pipeline Steel," Wear, **302**(1–2), pp. 1592–1601.

[11] Biswas, S., Cenna, A., Williams, K., and Jones, M., 2014, "Subsurface Behavior of Ductile Material by Particle Impacts and Its Influence on Wear Mechanism," Procedia Eng., **90**, pp. 160–165.

[12] Patel, M., Patel, D., Sekar, S., Tailor, P. B., and Ramana, P. V., 2016, "Study of Solid Particle Erosion Behaviour of SS 304 at Room Temperature," Procedia Technol., **23**, pp. 288–295.

[13] Islam, M. A., and Farhat, Z. N., 2014, "Effect of Impact Angle and Velocity on Erosion of API X42 Pipeline Steel Under High Abrasive Feed Rate," Wear, **311**(1–2), pp. 180–190.

[14] Özen, I., and Gedikli, H., 2019, "Solid Particle Erosion on Shield Surface of a Helicopter Rotor Blade Using Computational Fluid Dynamics," J. Aerosp. Eng., **32**(1), pp. 04018131.1–04018131.14.

[15] Chowdhury, M. A., Debnath, U. K., Nuruzzaman, D. M., and Islam, M. M., 2016, "Experimental Analysis of Aluminum Alloy Under Solid Particle Erosion Process," Proc. Inst. Mech. Eng. Part J J. Eng. Tribol., **230**(12), pp. 1516–1541.

[16] Yildiran, Y., Avcu, E., Sahin, A. E., Fidan, S., Yetistiren, H., and Sinmazçelik, T., 2014, "Effect of Particle Impact Angle, Erodent Particle Size and Acceleration Pressure on the Solid Particle Erosion Behavior of 3003 Aluminum Alloy," Acta Phys. Pol. A, **125**(2), pp. 523–525.

[17] Sahoo, R., Mantry, S., Sahoo, T. K., Mishra, S., and Jha, B. B., 2013, "Effect of Microstructural Variation on Erosion Wear Behavior of Ti-6Al-4V Alloy," Tribol. Trans., **56**(4), pp. 555–560.

[18] Fidan, S., Avcu, E., Karakulak, E., Yamanoglu, R., Zeren, M., and Sinmazcelik, T., 2013, "Effect of Heat Treatment on Erosive Wear Behaviour of Ti6Al4V Alloy," Mater. Sci. Technol. (United Kingdom), **29**(9), pp. 1088–1094.

[19] Vashishtha, N., Khatirkar, R. K., and Sapate, S. G., 2017, "Tribological Behaviour of HVOF Sprayed WC-12Co, WC-10Co-4Cr and Cr3C2−25NiCr Coatings," Tribol. Int., **105**, pp. 55–68.

[20] Bagci, M., and Imrek, H., 2011, "Solid Particle Erosion Behaviour of Glass Fibre Reinforced Boric Acid Filled Epoxy Resin Composites," Tribol. Int., **44**(12), pp. 1704–1710.

[21] Bagci, M., 2016, "Determination of Solid Particle Erosion with Taguchi Optimization Approach of Hybrid Composite Systems," Tribol. Int., **94**, pp. 336–345.

[22] Wensink, H., and Elwenspoek, M. C., 2002, "A Closer Look at the Ductile-Brittle Transition in Solid Particle Erosion," Wear, **253**(9–10), pp. 1035–1043.

[23] Routbort, J. L., and Scattergood, R. O., 1992, "Solid Particle Erosion of Ceramics and Ceramic Composites," Key Eng. Mater, **71**, pp. 23–50.

[24] Hao, Y., Feng, Y., and Fan, J., 2016, "Experimental Study Into Erosion Damage Mechanism of Concrete Materials in a Wind-Blown Sand Environment," Constr. Build. Mater, **111**, pp. 662–670.

[25] Sheldon, G. L., 1970, "Similarities and Differences in the Erosion Behavior of Materials," ASME J. Fluids Eng., **92**(3), pp. 619–626.

[26] Tilly, G. P., 1969, "Sand Erosion of Metals and Plastics: A Brief Review," Wear, **14**(4), pp. 241–248.

[27] Kleis, I., 1969, "Probleme Der Bestimmung Des Strahlverschleisses Bei Metallen," Wear, **13**(3), pp. 199–215.

[28] ASTM Standard, Designation: G76-95 (2000). "Standard Test Method for Conducting Erosion Tests by Solid Particle Impingement Using Gas Jets," 100 Bar Harbor Drive, West Conshohocken, PA 19428-2959, p. 1–5.

[29] Ruff, A. W., and Ives, L. K., 1975, "Measurement of Solid Particle Velocity in Erosive Wear," Wear, **35**(1), pp. 195–199.

[30] Li, K., Jiang, F., Xue, C., Yang, Y., and Ge, S., 2011, "Characteristics of Gobi Sand-Drift Along South Xinjiang Railway," J. Arid L. Resour. Environ., **25**(5), pp. 67–71.

[31] Jiang, F. Q., Li, Y., Li, K. C., Cheng, J. J., Xue, C. X., and Ge, S. C., 2010, "Study on Structural Characteristics of Gobi Wind Sand Flow in 100 Km Wind Area Along Lan-Xin Railway," Tiedao Xuebao/Journal China Railw. Soc., **32**(3), pp. 105–110.

[32] Bitter, J. G. A., 1963, "A Study of Erosion Phenomena Part I," Wear, **6**(1), pp. 5–21.

[33] Lindsley, B. A., and Marder, A. R., 1999, "The Effect of Velocity on the Solid Particle Erosion Rate of Alloys," Wear, **225–229**, pp. 510–516.

[34] Ou, G. F., Ye, H. J., Zheng, Z. J., Jin, H. Z., and Wang, C., 2016, "High-Speed Gas-Solid Two-Phase Flow Erosion of 1Cr9Mo Alloy," Gongcheng Kexue Xuebao/Chinese J. Eng., **38**(12), pp. 1747–1754.

[35] Algahtani, A., Neville, A., Shrestha, S., and Liskiewicz, T., 2013, "Erosion Resistance of Surface Engineered 6000 Series Aluminum Alloy," Proc. Inst. Mech. Eng. Part J. J. Eng. Tribol., **227**(11), pp. 1204–1214.

[36] Haider, G., Arabnejad, H., Shirazi, S. A., and Mclaury, B. S., 2017, "A Mechanistic Model for Stochastic Rebound of Solid Particles With Application to Erosion Predictions," Wear, **376–377**, pp. 615–624.

[37] Bellman, R., and Levy, A., 1981, "Erosion Mechanism in Ductile Metals," Wear, **70**(1), pp. 1–27.

[38] Finnie, I., 1960, "Erosion of Surfaces by Solid Particles," Wear, **3**(2), pp. 87–103.

[39] Tilly, G. P., 1973, "A Two Stage Mechanism of Ductile Erosion," Wear, **23**(1), pp. 87–96.

[40] Levy, A. V., 1988, "The Erosion-Corrosion Behavior of Protective Coatings," Surf. Coat. Technol., **36**(1), pp. 387–406.